Journal of Materials Chemistry A

Accepted Manuscript

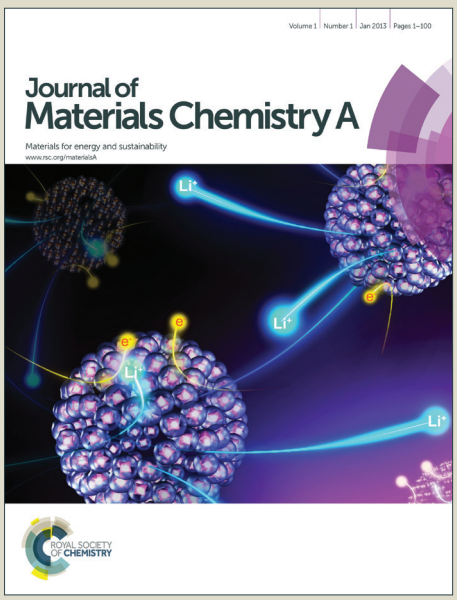

This is an *Accepted Manuscript*, which has been through the Royal Society of Chemistry peer review process and has been accepted for publication.

Accepted Manuscripts are published online shortly after acceptance, before technical editing, formatting and proof reading. Using this free service, authors can make their results available to the community, in citable form, before we publish the edited article. We will replace this *Accepted Manuscript* with the edited and formatted *Advance Article* as soon as it is available.

You can find more information about *Accepted Manuscripts* in the Information for Authors.

Please note that technical editing may introduce minor changes to the text and/or graphics, which may alter content. The journal's standard Terms & Conditions and the Ethical guidelines still apply. In no event shall the Royal Society of Chemistry be held responsible for any errors or omissions in this *Accepted Manuscript* or any consequences arising from the use of any information it contains.

ROYAL SOCIETY OF CHEMISTRY

www.rsc.org/materialsA

Cite this: DOI: 10.1039/c0xx00000x

www.rsc.org/xxxxxx

ARTICLE TYPE

Improving the performance of PEDOT-PSS coated sulfur@activated porous graphene composite cathodes for lithium-sulfur batteries

Han Li,[a] Minqiang Sun,[a] Tao Zhang,[a] Yuqian Fang[a] and Gengchao Wang*[a]

Received (in XXX, XXX) Xth XXXXXXXXX 20XX, Accepted Xth XXXXXXXXX 20XX
DOI: 10.1039/b000000x

A novel PEDOT-PSS coated sulfur@activated porous graphene composite (PEDOT/S@*a*PG) is prepared by the impregnation of sulfur with the *a*PG and encapsulation with PEDOT-PSS as the cathode material for lithium-sulfur batteries. The abundant nanopores and large surface area for *a*PG can provide intimate contact and strong interaction with S species. Furthermore, the conductive PEDOT-PSS layer can facilitate the charge transportation and prevent the dissolution of polysulfides. As a result, the as-prepared PEDOT/S@*a*PG composite cathode with a sulfur content of about 60.1 % shows higher specific discharge capacity (1198 mAh g^{-1} at 0.1 C) in the first cycle and good cycling stability, retaining a reversible capacity of 845 mAh g^{-1} after 200 cycles. Moreover, the PEDOT/S@*a*PG cathode also exhibits excellent rate capability, showing a high reversible capacity of 718 mAh g^{-1} at 2 C.

1. Introduction

Nowadays, the rechargeable lithium-sulfur (Li-S) battery has gained considerable attention due to its high theoretical specific capacity (1675 mAh g^{-1}) and high specific energy (2600 Wh kg^{-1}), which makes it very attractive as power source for applications in electric vehicles and efficient storage for renewable energy.[1-3] In addition, sulfur as a cathode active material has the advantages of natural abundance, inexpensive, and environmentally benign. Unfortunately, the shortcomings including the low electrical conductivity (5×10^{-30} S cm^{-1}) of elemental sulfur, the dissolution of polysulfides into electrolytes, and the volume variation of the cathode material during charge/discharge cause a poor cycle life and prevent the practical application of Li-S battery.[4-7]

In order to overcome the above-mentioned drawbacks, various carbonaceous materials such as carbon black,[8-10] porous carbon,[11-17] carbon nanotube,[18-24] carbon sphere[7,25,26] and graphene/graphene oxide[27-41] have been used as support materials of sulfur cathode. As a two-dimensional structure of carbon atoms, graphene with high electrical conductivity, large surface area, superior chemical and thermal stability[42,43] is an ideal candidate for electrochemical energy storage.[44] The sulfur/graphene composites are prepared mainly through the melt diffusion strategy or solution-based reaction-deposition to form sulfur@graphene particles.[45] According to noteworthy reports, Zhang's group showed that the oxygen-containing groups on graphene surface have adsorbing ability to anchor S atoms and provide polysulfides occupying sites.[29,46] Meanwhile, the introduction of graphene sheets could improve the electrochemical performance and the utilization of sulfur. However, the graphene sheets with open structure are not effective to confine the polysulfides from dissolving out of the composites, which initiate the "shuttle" problem.[47,48] As demonstrated by Li et al., a thermally exfoliated graphene nanosheet/sulfur (TG-S) with the laminar structure was prepared, but the capacity decayed quickly to 421 mAh g^{-1} after 100 cycles at 0.2 A g^{-1} in the absence of a RGO coating.[30] Cao et al. have also synthesized a sandwich-type functionalized graphene sheet-sulfur nanocomposite, which showed ~52 % retention of its initial capacity after 50 cycles at 0.1 C when no Nafion coating was applied.[49]

The surface coating with conductive polymers has been proved to be another effective way to improve the cycle life of sulfur cathode.[50-58] Cui et al. reported a PEDOT-PSS coated CMK-3/sulfur cathode with the capacity retention increasing from ~60 %/100 cycles to ~85 %/100 cycles and the coulomb efficiency increasing from 93% to 97%.[52] Gao and his co-workers prepared a polyaniline-coated sulfur/carbon composite, which showed ~60 % retention of the discharge after 200 cycles at an ultrahigh rate (10 C).[54] In a word, the coating layer of conductive polymers promises rapid high-rate charge transfer and hinders the loss of sulfur, which is beneficial to improve the electrochemical performance and cyclability.

Herein, the activated porous graphene (*a*PG)[59,60] was prepared by chemical oxidation, thermal reduction assisted by chemical foaming, and KOH activation using natural graphite.[61] S@*a*PG composite was further synthesized through melt diffusion strategy, and then a poly(3,4-ethylenedioxythiophene)-poly(styrene sulfonate) (PEDOT-PSS) layer was coated onto the surface of the S@*a*PG composite. The preparation process is illustrated in Scheme 1. The *a*PG with abundant nanopores and high conductivity not only is beneficial to firmly deposit nano-scale S species, but also serves as conductive substrate for electron transport. Meanwhile, the conductive PEDOT-PSS layer

Journal of Materials Chemistry A Accepted Manuscript

can effectively impede the dissolution of polysulfides and facilitate charge transport. As a result, the as-prepared PEDOT-PSS coated S@*a*PG (PEDOT/S@*a*PG) composite exhibits superior rate capability and good cycle life.

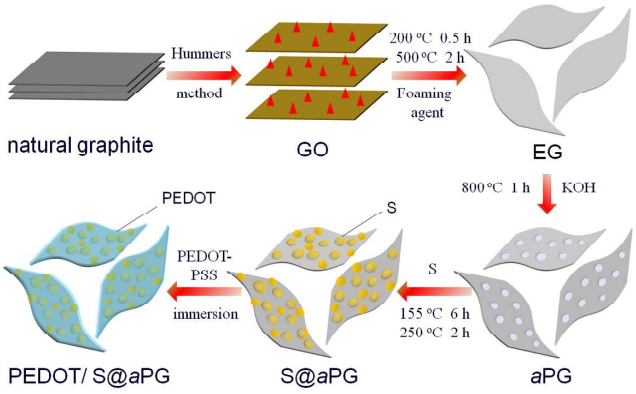

Scheme 1 Schematic diagram of the formation of the PEDOT/S@*a*PG composite

2. Experimental

2.1 Preparation of *a*PG

Graphite oxide (GO) was synthesized from natural graphite powder (500 mesh Shanghai Yifan Graphite Co. Ltd.) using modified Hummers method.[62] *a*PG derived from GO was synthesized by thermal reduction assisted by foaming agent and activation with KOH according to our previous report.[61] Typical procedure was as follows: Briefly, 0.5 g of GO was dispersed in ethanol solution of 0.5 g salicylic acid (SA) to obtain uniform slurry. The superfluous SA was removed by filtering the mixture, followed by drying at 60 °C overnight. The dry GO/SA mixture was first heated at 200 °C for 30 min, then the temperature was ramped at 10 °C min^{-1} to 500 °C and held there for 2 h under mixed gas flow of argon and hydrogen (4/1, v/v) to obtain exfoliated graphene (EG). Finally, the EG and KOH were mixed with a weight ratio of 1:8 and heated to 800 °C at a ramp of 10 °C min^{-1} and held there for 1 h in a tube furnace under argon atmosphere. The as-prepared sample was boiled in 0.1 M HCl for 1 h and then washed with copious deionized water to neutral.

2.2 Preparation of PEDOT-PSS

2.2 g poly(sodium-*p*-styrenesulfonate) (PSS, Aladdin reagent) was first dissolved in 100 mL deionized water with continuous stirring. Then 0.75 g 3,4-ethylenedioxythiophene (EDOT, Sigma-Aldrich) was added to the above solution and stirred for an extra 15 min. Afterward, 1.7 g of ammonium persulfate (dissolved in 200 mL of deionized water) was dropped into the as-obtained solution while its pH was adjusted to 2 with HCl solution. The reaction was kept at 25 °C for 24 h with continuous stirring. The resulting PEDOT-PSS solution was dialyzed for 3 days using dialysis membrane (molecular weight cutoff, 3500) in deionized water, which was replaced with fresh deionized water frequently to remove salts and oligomers.

2.3 Preparation of S@*a*PG composite

The as-prepared *a*PG and sulfur powder (Aladdin reagent, purity > 99.999 %) were thoroughly mixed with a mass ratio of *a*PG:S = 1:8 in a agate mortar for 1 h. The mixture was sealed in quartz tube and held at 155 °C for 6 h to ensure a complete migration of melted sulfur into the interior porous structure of *a*PG. Then the temperature was increased to 250 °C for 2 h under argon to remove bulk sulfur and the S@*a*PG composite was obtained.

2.4 Preparation of PEDOT-PSS coated S@*a*PG composite

0.1 g S@*a*PG composite was added into 20 mL PEDOT-PSS solution (0.5 mg/mL) for 1 h with ultrasonic stirring to obtain well-dispersed suspension. Then the solution was centrifuged and washed with deionized water and acetone to isolate the precipitate. Finally, the precipitate was dried at 60 °C for 12 h to obtain the PEDOT-PSS coated S@*a*PG (PEDOT/S@*a*PG) composite.

2.5 Characterization

The morphologies of the samples were characterized by the field-emission scanning electron microscopy (FESEM, Hitachi S-4800) and transmission electron microscopy (TEM, JEOL JEM-1400; HRTEM, JEOL JEM-2100). The elemental mapping analysis was obtained by an energy dispersive spectrometer (EDS, QUANTAX 400-30). X-ray photoelectron spectroscopy (XPS) was carried out in a thermo scientific ESCALAB 250Xi X-ray photoelectron spectrometer equipped with amonochromatic Al Kα X-ray source (1486.6 eV). Fourier transform infrared spectra (FTIR) were obtained through a Nicolet 5700 spectrometer using KBr sample pellets. Raman spectra were recorded with Renishaw inVia+Reflex using a 50 mW He-Ne laser operated at 514 nm. Powder X-ray diffraction (XRD) patterns were performed in a Rigaku D/Max 2550 VB/PC X-ray diffractometer using Cu (Kα) radiation with the 2θ-angle recorded from 3-70°. Sulfur ratio in the composite was ascertained by a TGA/SDTA/851E analyzer under N_2 flow at a heating rate of 10 °C min^{-1}. Nitrogen adsorption-desorption isotherms were performed using a Micromeritics ASAP 2020 analyzer at 77 K. The specific surface area and the pore size distribution were calculated using the BET and slit/cylindrical nonlocal DFT (NLDFT) methods, respectively. The electrical conductivities of the samples were determined by a SX 1934 four-probe instrument using compressed pellets at room temperature.

2.6 Cells assemble and electrochemical measurements

The cathodic electrodes were prepared by mixing active materials (80 wt.%), acetylene black (10 wt.%) and binder (10 wt.% LA132, dissolved in deionized water/ethanol mixed solution) to form slurries. Then the slurries were homogeneously coated onto aluminum foil current collectors. The electrodes were dried at 60 °C for 12 h under vacuum. Subsequently, the electrodes were cut into disks with a diameter of 12 mm. The typical loading of sulfur was approximately 1 mg cm^{-2}. The CR2032 coin-type cells were fabricated using the working electrodes and lithium metal foil as the counter electrode. The porous polypropylene membrane (Celgard 2400) was used as the separator. The electrolyte was 1 M bis-(trifluoromethane)sulfonimide lithium (LiTFSI) in dimethoxyethane (DME) and dioxolane (DOL) (1:1, v/v) with 1 % $LiNO_3$ as an additive. The coin cells were assembled in an argon atmosphere glove box. The electrolyte volume added to the test cells was constant at 100 μl. The

Journal of Materials Chemistry A Accepted Manuscript

This journal is © The Royal Society of Chemistry [year]

galvanostatic charge/discharge tests were carried out on a LAND CT2001A battery tester between 1.5 and 3.0 V (versus. Li/Li^+). The cyclic voltammetry (CV) (scan rate: 0.1 mVs^{-1}; cut-off voltage: 1.5-3.0 V) and electrochemical impedance measurements (frequency range: 0.01-100,000 Hz; amplitude: 5 mV) were conducted on a CHI660D electrochemical workstation, respectively.

3. Results and discussion

The morphologies of EG and *a*PG are characterized by FE-SEM and HR-TEM analysis. As shown Fig. 1a, EG exhibits a loose architecture stacked by wrinkled laminar graphene sheets, deriving from a large volume expansion in foaming process. After activation of KOH, the *a*PG still displays the key feature of well-exfoliated thin sheets (Fig. 1b). The high magnification FESEM and HR-TEM images (Fig. 1c and 1d) demonstrate that the surface of *a*PG is rough and irregular (indicated by the arrows), while the HR-TEM image of EG exhibits a smoother surface (Fig. S1, ESI†). This may be ascribed to the etching of KOH during the activation process. The surface structure of *a*PG is further characterized by nitrogen adsorption/desorption isotherms and the result of pore size distribution is based on a hybrid nonlocal density functional theory (NLDFT). As shown in Fig. 1e, the *a*PG shows a strong adsorption of micropores below low relative pressure ($P/P_0<0.1$). The obvious hysteresis loop in the range of 0.4~0.99 P/P_0 indicates the presence of mesopores, which can be derived from the activation of KOH and the restack of wrinkled laminar sheets. The BET surface area of *a*PG is 1420 $m^2 g^{-1}$ with a total pore volume of 1.37 $cm^3 g^{-1}$. BJH analysis for *a*PG shows a sharp peak around 2 nm size with a broad pore distribution ranging from 1.7~10 nm (Fig. 1f). This result indicates that the sample has a hierarchically porous structure of micro- and mesopores, which consistents with the above FE-SEM and HR-TEM observation. Notably, the large surface of *a*PG is beneficial for improving the load of active material and providing channels for the transport and diffusion of Li ions. Simultaneously, the hierarchically porous structure can provide better contact of elemental sulfur onto the graphene surface and confine sulfur and polysulfides effectively.

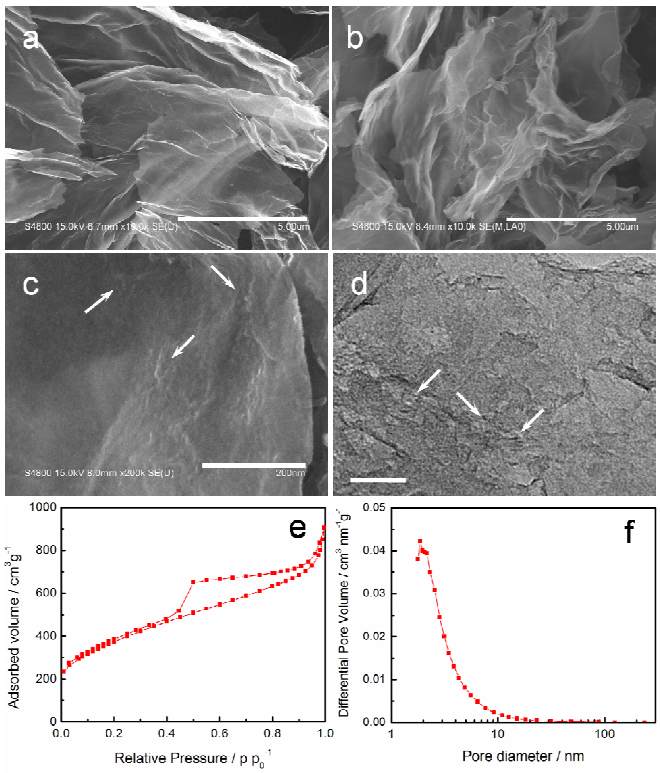

Fig. 1 (a) Low magnification FE-SEM image of EG (scale bars: 5 μm). (b) Low (scale bars: 5 μm) and (c) high magnification FE-SEM images of *a*PG (scale bars: 200 nm). (d) HR-TEM image of *a*PG (scale bars: 50 nm). (e) N_2 adsorption/desorption isotherm, and (f) Pore size distribution curve of *a*PG.

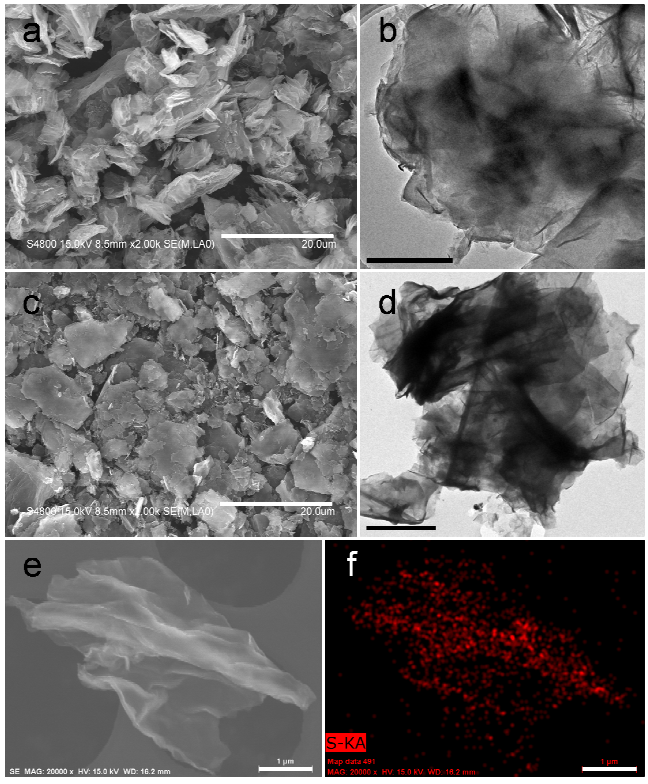

Fig. 2 FE-SEM images of (a) S@*a*PG (scale bars: 20 μm) and (c) PEDOT/S@*a*PG (scale bars: 20 μm). TEM images of (b) S@*a*PG (scale bars: 1 μm) and (d) PEDOT/S@*a*PG (scale bars: 2 μm). The EDS sulfur mapping analysis of (e), (f) S@*a*PG (scale bars: 1 μm).

FE-SEM and TEM are also performed to observe the morphologies of S@*a*PG and PEDOT/S@*a*PG composites. As shown in Fig. 2a, the S@*a*PG composite exhibits wrinkled aggregate structure without bulk sulfur. The energy dispersive spectroscopic (EDS) mapping analysis clearly reveals that the elemental sulfur disperses on the surface of *a*PG homogeneously (Fig. 2e and Fig. 2f). The TEM image also demonstrates that a thin layer of S is coated on the wrinkled *a*PG sheets after heat treatment (Fig. 2b). The FE-SEM image of PEDOT/S@*a*PG demonstrates that the edge of the composite becomes fuzzier and the wrinkled structure becomes unobvious due to the coating by the PEDOT-PSS layer (Fig. 2c). The TEM image of PEDOT/S@*a*PG shows that the surface of composite becomes dark (Fig. 2d), which is ascribed to the introduction of the PEDOT-PSS layer. To further confirm the presence of PEDOT-PSS, the FTIR spectra are measured (Fig. S2, ESI†). In the case

Journal of Materials Chemistry A Accepted Manuscript

of PEDOT/S@*a*PG, the bands at 837, 1033, 1087 and1189 cm^{-1} are assigned to the C-S stretching vibration in the thiophene rings, the S=O stretching vibration of SO_3^- groups, and the vibration modes of the ethylenedioxy groups, respectively.[63] These results indicate the existence of PEDOT-PSS layer, which can not only improve the reaction kinetics for facilitating transportation of charge, but also inhibit the dissolution of polysulfides effectively.[64,65]

The XRD patterns offer the information about crystal structures of the samples. As shown in Fig. 3, elemental sulfur exhibits several sharp peaks from 15° to 60°, indicating its good crystal structure. It is found that the *a*PG has a broad peak around 25° corresponding to the diffraction of the (002) plane of the graphene sheets, indicating its typical amorphous structure. In the S@*a*PG composite, the sharp peaks related to crystal sulfur are observed. However, the intensity of the diffraction peaks decreases significantly, which suggests that a partial amount of sulfur becomes amorphous and is parasitized inside of hierarchically porous structure of *a*PG. For the PEDOT/S@*a*PG composite, all diffraction peaks of crystal sulfur further diminish, which is attributed to that the surface of S@*a*PG composite is covered by the PEDOT-PSS thin layer.

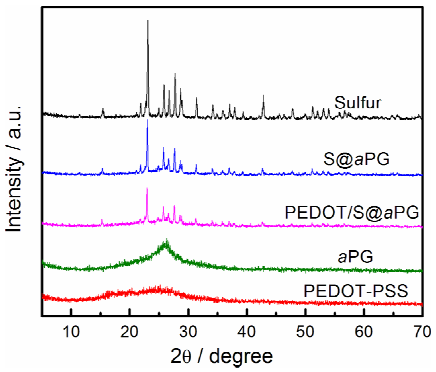

Fig. 3 XRD patterns of sulfur, S@*a*PG, PEDOT/S@*a*PG, *a*PG and PEDOT-PSS.

The structural information of the samples is further evaluated by Raman spectroscopy (Fig. 4). The spectrum of the elemental sulfur shows the three sharp peaks (centered at 155, 220 and 476 cm^{-1}) corresponding to characteristic signals of S_8 species.[66] For the S@*a*PG composite, the characteristic peaks of elemental sulfur (152, 219 and 473 cm^{-1}) and the *a*PG (G band at 1590 cm^{-1} and D band at 1353 cm^{-1}) are observed. Additionally, there are three new peaks at 318, 374 and 394 cm^{-1} for the S@*a*PG composite (Fig. 4b), which can be attributed to C-S in plane bending, C-S deformation and S-S stretching vibrations, respectively.[67,68] This indicates that the presence of chemical interaction between the elemental sulfur and the *a*PG, which can confine the dissolution of S species into electrolyte and facilitate the cycling stability of active material. However, there only exists the characteristic peaks of the *a*PG (1590 and 1353 cm^{-1}) for the PEDOT/S@*a*PG composite and the peaks at the range of 150~500 cm^{-1} are not obvious, which may be caused by the coating of PEDOT-PSS thin layer on the surface of S@*a*PG. Furthermore, the intensity ratio of the D and G bands (I_D/I_G) calculated from the band area is 1.49 in S@*a*PG, much lower than that of *a*PG (I_D/I_G = 1.62). The decreasing of I_D/I_G for S@*a*PG demonstrates the improvement of the degree of disorder, which suggests that the incorporation of sulfur during the impregnation process can effectively reduce some of the functional groups and repair lattice defects. This is beneficial to the electrical conductivity of the S@*a*PG composite. To better investigate the change before and after sulfur impregnation, the conductivities of pure *a*PG and *a*PG after removel of sulfur from S@*a*PG are measured, and the values are 33.2 and 46.9 S cm^{-1}, respectively. This result is consistent with above analysis.

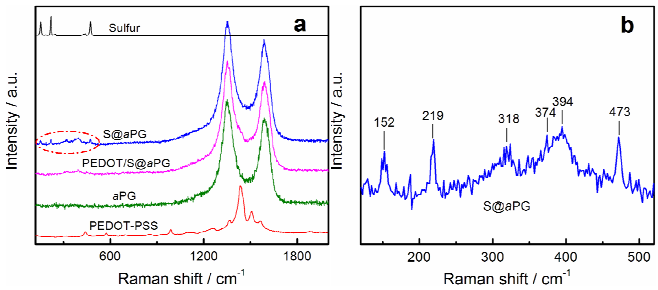

Fig. 4 (a) Raman spectra of sulfur, S@*a*PG, PEDOT/S@*a*PG, *a*PG and PEDOT-PSS. (b) The magnification of the area marked by the red frame.

To further investigate the interaction between the elemental sulfur and the *a*PG in S@*a*PG, the XPS analysis is employed. As shown in Fig. 5a, the C *1s* of *a*PG shows a main peak at 284.6 eV, which corresponds to the *sp*2 carbon (C=C) in the aromatic rings. The higher binding energy peaks at 285.5, 286.7 and 288.3 eV can be attributed to the carbon species of C-OH, C-O-C and C=O groups, respectively.[69] In comparison, the relative intensities of different functional groups in S@*a*PG are weaker than those in *a*PG, implying that the *a*PG is partially reduced after the incorporation of sulfur. Moreover, the peak at 285.4 eV with the shift of ~0.1eV can be attributed to the formation of C-S, indicating the existence of chemical bonding between the *a*PG and sulfur.[40,41] Fig. 5b displays the S *2p* spectrum for the S@*a*PG composite. The peaks at 165.0 and 163.8 eV can be assigned to the S $2p_{1/2}$ and S $2p_{3/2}$ spin-orbit levels of elemental sulfur. A broad peak centered at 168.5 eV is also observed, which can be ascribed to the C-S for the strong interaction between sulfur and *a*PG.[70] This chemical interaction is in good accordance with our Raman results above, which can bring an adsorbing ability to immobilize S atoms and suppress the dissolving of polysulfides during cycling. In addition, the oxygen-containing groups on *a*PG surface also provide polysulfides occupying sites as a viable enhancer of reversibility by stabilizing the intermediates.[29,46,71]

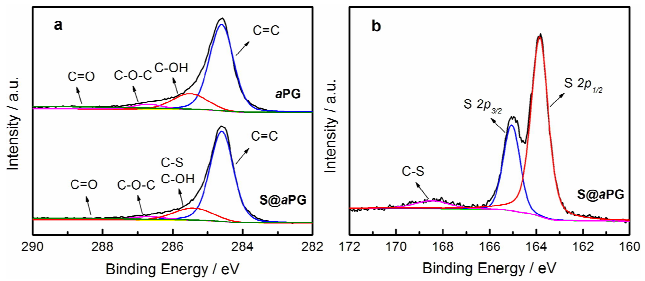

Fig. 5 XPS spectra of (a) C *1s* for *a*PG and S@*a*PG and (b) S *2p* for S@*a*PG.

To determine the sulfur contents in the composites, TGA is performed in Fig. 6. The weight of S@*a*PG begins to decrease

This journal is © The Royal Society of Chemistry [year]

Journal of Materials Chemistry A Accepted Manuscript

from the melting point of pure sulfur (i.e. 115 °C), which can be ascribed to the evaporation of sulfur from the surface, and the weight loss is continuous until the sample is heated to over 310 °C. The sulfur content is 65.7 % in the S@*a*PG composite and a hysteretic weight loss profile appears compared with elemental sulfur, indicating the existence of intimate interaction between sulfur and *a*PG. For the PEDOT/S@*a*PG composite, the weight loss peak of sulfur shifts to the higher temperature range of 150-320 °C with a much lower evaporation rate, inferring that the incorporation of PEDOT-PSS triggers a strong confinement effect for improving the stability of sulfur, and the sulfur loading of PEDOT/S@*a*PG is 60.1 %.

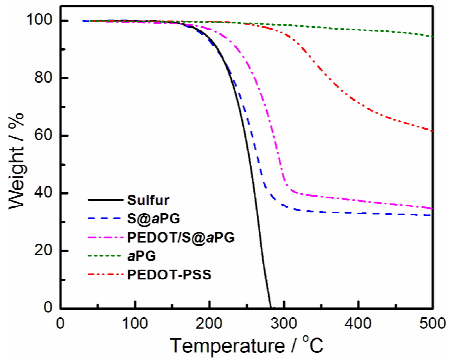

Fig. 6 Thermogravimetric curves for sulfur, S@*a*PG, PEDOT/S@*a*PG, *a*PG and PEDOT-PSS.

To evaluate the electrochemical performance of S@*a*PG and PEDOT/S@*a*PG as the cathodic electrodes, the cyclic voltammetry and galvanostatic charge/discharge can be employed. The typical CV curves for the S@*a*PG and PEDOT/S@*a*PG in the potential window of 1.5−3.0 V at a scan rate of 0.1 mV s^{-1} are shown in Fig. 7. For the S@*a*PG composite, two remarkable reduction peaks at 2.26 V and 2.0 V appear during the first cathodic scan, which associate with the conversion of elemental sulfur to soluble lithium polysulfides (Li_2S_n, $4 \leq n < 8$) and the reduction of lithium polysulfides to insoluble Li_2S_2 and Li_2S. In the anodic scan, only one sharp oxidation peak is observed in the potential of 2.4 V, which corresponds to the conversion of Li_2S_2 and Li_2S to the high-order lithium polysulfide (Li_2S_8). However, the cathodic peaks positively shifted to 2.34 V and 2.04 V after the first cycle, while the anodic peaks are almost at the same position. Such a result is probably due to the fact that the active material is well trapped and suppressed by the strong interaction between the *a*PG matrix and S species. So the electrochemical reactions in the first cathodic scan need to overcome the strong adsorption energy between the *a*PG and active material, resulting in the polarization towards a lower potential.[72] For the PEDOT/S@*a*PG composite, two pairs of redox peaks can be observed during the cycles. The reduction peaks at 2.37 V and 2.04 V correspond to the similar transformation of S@*a*PG, while the cathodic peaks at 2.36 V and 2.4 V can be assigned to the formation of the low-order lithium polysulfide (Li_2S_4) and the high-order lithium polysulfide (Li_2S_8), respectively. Notably, there are no major potential or current changes for the CV curves of PEDOT/S@*a*PG after the first cycle, indicating that this composite has stable electrochemical performance. In addition, the shifts of the cathodic peaks to the higher potentials and the anodic peaks to the lower potentials in PEDOT/S@*a*PG suggest that the introduction of conductive PEDOT-PSS can cause a reduction of polarization and an improvement of electrochemical performance.

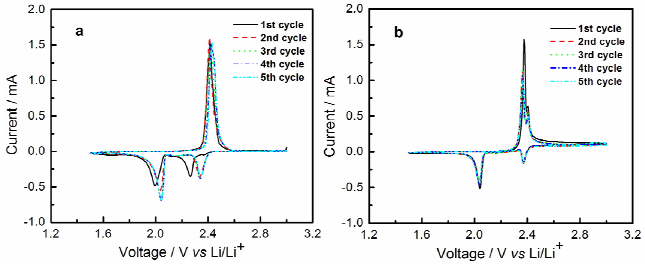

Fig. 7 Cyclic voltammograms at a scan rate of 0.1 mV s^{-1} of (a) S@*a*PG and (b) PEDOT/S@*a*PG.

Fig. 8a and 8b present the discharge and charge profiles of S@*a*PG and PEDOT/S@*a*PG composites at various rates after the initial activation process, respectively. The discharge curves for the two composites exhibit typical two-plateau behavior of a sulfur cathode even at the high current rates, corresponding to the formation of the low-order lithium polysulfide at about 2.3 V and insoluble Li_2S_2 and Li_2S at about 2.1 V. Moreover, the voltage gap between discharge and charge plateau of the PEDOT/S@*a*PG is much smaller than that of the S@*a*PG with the increasing of the rate, indicating the lower polarization and the better electrochemical performance. In addition, a small plateau can be detected at about 1.6 V for both of the discharge profiles at 0.1 C, it could be attributed to the irreversible reduction of $LiNO_3$ at potentials lower than 1.7 V.[73,74] The corresponding rate capability of S@*a*PG and PEDOT/S@*a*PG at various rates is shown in Fig. 8c. The PEDOT/S@*a*PG delivers a discharge capacity of 1180 mAh g^{-1} after the activation of the first cycle at 0.1 C (the capacity is calculated based on the mass of sulfur). With the increasing of the current density to 0.2 C, 0.5 C, 1 C and 2 C, the PEDOT/S@*a*PG obtains the satisfactory capacities of 971, 872, 798 and 718 mAh g^{-1}, respectively. When PEDOT/S@*a*PG is discharged at 0.1 C again, a reversible capacity of 890 mAh g^{-1} can be obtained, suggesting the perfect stability under different rates. In the case of S@*a*PG, the discharge capacities of 927 mAh g^{-1} and 746 mAh g^{-1} are obtained at a rate of 0.1 C in the 2nd and 11th cycle. Subsequent cycle at 0.2 C, 0.5 C, 1 C and 2 C show the reversible capacities of 717, 573, 483 and 395 mAh g^{-1}, respectively. When the current is abruptly switched from 2 C to 0.1 C again, a reversible capacity of 586 mAh g^{-1} can only be recovered. These results are revealed as the discharge and charge profiles in Fig. 8a and 8b. It can be found that PEDOT/S@*a*PG shows better rate performance than that of S@*a*PG, demonstrating the assistance of the conductive PEDOT-PSS in facilitating the transportation of charge and suppressing the dissolution of polysulfides.

The cycling performance of the S@*a*PG and PEDOT/S@*a*PG composites is demonstrated in Fig. 8d. In the case of the S@*a*PG, the discharge capacity of the first cycle at 0.1 C is 1042 mAh g^{-1}. A capacity of 455 mAh g^{-1} is retained after 200 cycles corresponding to a capacity retention of 43.6 % of its highest capacity (a decay of 0.282 % per cycle). The S@*a*PG cell maintains a high coulombic efficiency and the average value is above 99 %. To demonstrate the possible structural benefit of S@*a*PG composite, a S@EG sample is prepared as the same

Journal of Materials Chemistry A Accepted Manuscript

conditions without any KOH activation and the loading mass of sulfur is about 65 %. As shown in Fig. S3, the initial discharge capacity of S@EG is 989 mAh g^{-1}, which is slightly lower than that of S@*a*PG. After 200 cycles, the S@EG cell delivers a reversible discharge capacity of 352 mAh g^{-1} (a capacity retention of 35.6 %). The capacity decay is as high as 0.322 % per cycle and the average coulombic efficiency is about 98 %. The improved cycling stability of S@*a*PG can be attributed to the novel structure with a large number of micro- and mesopores and the strong interaction between the *a*PG and the S species. As a result, the active material can keep an intimate contact with *a*PG due to the large surface area to obtain a high capacity and the matrix owns the absorbent ability to suppress lithium polysulfides for their dissolution into the electrolyte during prolonged cycling. For the PEDOT/S@*a*PG, the initial discharge capacity is as high as 1198 mAh g^{-1}. After the rapid initial decay, the discharge capacity stabilizes at 957 mAh g^{-1} after 20 more cycles and a reversible capacity of 845 mAh g^{-1} can be obtained even after 200 cycles, corresponding to the capacity retention of 70.5 % (a decay of only 0.148 % per cycle). The average coulombic efficiency of the cell for 200 cycles is 99.5 %. To gain further information of the impact of the PEDOT-PSS coating on the polysulfide shuttle, the cycling test of PEDOT/S@*a*PG without $LiNO_3$ in the electrolyte is performed. As shown in Fig. S4, the sample delivers an initial discharge capacity of 1213.8 mAh g^{-1} and a reversible discharge capacity of 744.2 mAh g^{-1} after 200 cycles. The coulombic efficiency of 95 % can be achieved during cycles. The excellent electrochemical performance of PEDOT/S@*a*PG has close relation to the synergistic contribution from the conductive PEDOT-PSS layer and the *a*PG mentioned above. The PEDOT-PSS on the surface of the S@*a*PG can effectively facilitate the transportation of ions and electrons to improve the reaction kinetics for the high utilization of sulfur. Simultaneously, the PEDOT-PSS plays an important role to build a barrier to retard the dissolution of polysulfides during the cycles for the physical confinement and chemical interaction with S species,[65] resulting in the excellent cycling performance of PEDOT/S@*a*PG.

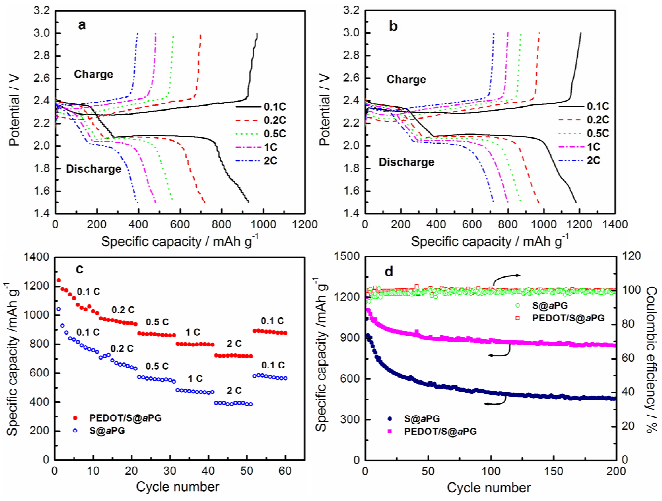

Fig. 8 Electrochemical preformance of S@*a*PG and PEDOT/S@*a*PG. (a) The discharge and charge profiles of S@*a*PG at various rates. (b) The discharge and charge profiles of PEDOT/S@*a*PG at various rates. (c) Rate capability at various rates of S@*a*PG and PEDOT/S@*a*PG. (d) Cycling performance and coulombic efficiency of S@*a*PG and PEDOT/S@*a*PG.

To further clarify the improving effect of introducing PEDOT-PSS on the electrochemical performance, the electrochemical impedance spectroscopy (EIS) tests of the S@*a*PG and PEDOT/S@*a*PG electrodes are also conducted before and after 200 cycles. As presented in Fig. 9, two composites exhibit a depressed semicircle in the high frequency region, corresponding to the charge-transfer resistance (R_{ct}). It is seen that PEDOT/S@*a*PG has a much smaller R_{ct} (75 Ω) than that of *S*@*a*PG (300 Ω), which can be attributed to the improved conductivity. After cycling for 200 times, the increasing rate of R_{ct} of PEDOT/S@*a*PG is much lower than that of S@*a*PG, which further supports the conclusion that PEDOT/S@*a*PG exhibits good cycling stability compared with S@*a*PG.

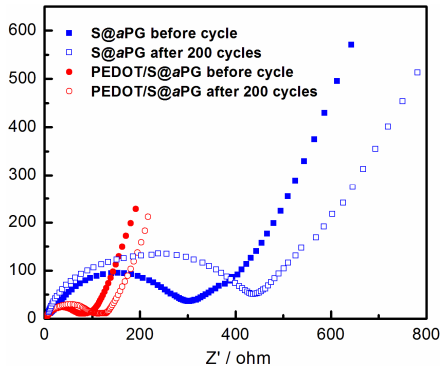

Fig. 9 Nyquist plots of the S@*a*PG and PEDOT/S@*a*PG electrodes before and after 200 cycles.

Based on the above analysis, a PEDOT/S@*a*PG composite electrode with good rate capability and cycling stability is successfully constructed. The remarkable electrochemical performance of the PEDOT/S@*a*PG could be attributed to following three factors. Firstly, the *a*PG after activation with a large number of micro- and mesopores possess an intimate contact with element sulfur due to the large surface area, which is beneficial to improve the loading mass and utilization of sulfur and provide channels for the transport and diffusion of Li ions. Secondly, the incorporation of sulfur with *a*PG during the impregnation process can effectively remove the functional groups and repair lattice defects to some extent for the enhancement of the conductivity and facilitate the formation of the strong interaction between the *a*PG and S species, which provides an adsorbing ability to anchor the polysulfides. Finally, the conductive PEDOT-PSS layer on the surface of the S@*a*PG can effectively facilitate the charge transportation to improve the reaction kinetics of the sulfur and build a barrier to retard the dissolution of polysulfides during the cycling process.

4. Conclusions

In summary, we have successfully synthesized a novel PEDOT/S@*a*PG composite cathode for lithium-sulfur batteries. The PEDOT/S@*a*PG composite cathode delivers high discharge specific capacity at different current rates (1198, 971, 872, 798 and 718 mAh g^{-1} at 0.1 C, 0.2 C, 0.5 C, 1 C and 2 C, respectively) and good capacity retention of 70.5 % after 200 cycles at 0.1 C. The excellent performance of PEDOT/S@*a*PG is attributed to the introduction of the *a*PG matrix and PEDOT-PSS layer. The hierarchically porous structure of *a*PG can provide intimate

Journal of Materials Chemistry A Accepted Manuscript

This journal is © The Royal Society of Chemistry [year]

contact and strong interaction with S species. The conductive PEDOT-PSS layer can remarkably facilitate the charge transportation and increase the kinetic inhibition of polysulfides to diffusion. The as-prepared PEDOT/S@*a*PG composite may be a promising cathode material for high-performance lithium-sulfur batteries. Based on this work, we will further improve the preparation technology and enhance the encapsulation efficiency to obtain a better cathodic electrode material for energy storage applications.

Acknowledgments

We greatly appreciate the financial supports of National Natural Science Foundation of China (51173042), Fundamental Research Funds for the Central Universities, Shanghai Municipal Science and Technology Commission (12nm0504102).

Notes and references

[a] *Key Laboratory for Ultrafine Materials of Ministry of Education, Shanghai Key Laboratory of Advanced Polymeric Materials, School of Materials Science and Engineering, East China University of Science and Technology, Shanghai 200237, P.R.China. E-mail: gengchaow@ecust.edu.cn*

1 P. G. Bruce, B. Scrosati and J. M. Tarascon, *Angew. Chem. Int. Ed.*, 2008, **47**, 2930-2946.
2 J. M. Tarascon and M. Armand, *Nature*, 2001, **414**, 359-367.
3 M. Winter and R. Brodd, *Chem. Rev.*, 2004, **104**, 4245-4269.
4 S. E. Cheon, S. S. Choi, J. S. Han, Y. S. Choi, B. H. Jung and H. S. Lim, *J. Electrochem. Soc.*, 2004, **151**, A2067-A2073.
5 Y. S. Choi, S. Kim, S. S. Choi, J. S. Han, J. D. Kim, S. E. Jeon and B. H. Jung, *Electrochim. Acta*, 2004, **50**, 833-835.
6 Y. V. Mikhaylik and J. R. Akridge, *J. Electrochem. Soc.*, 2004, **151**, A1969-A1976.
7 N. Jayaprakash, J. Shen, S. S. Moganty, A. Corona and L. A. Archer, *Angew. Chem., Int. Ed.*, 2011, **50**, 5904-5908.
8 J. L. Wang, J. Yang, J. Y. Xie, N. X. Xu and Y. Li. *Electrochem. Commun.*, 2002, **4**, 499-502.
9 Y. S. Su and A. Manthiram, *Electrochim. Acta*, 2012, **77**, 272-278.
10 G. C. Li, J. J. Hu, G. R. Li, S. H. Ye and X. P. Gao, *J. Power Sources*, 2013, **240**, 598-605.
11 X. L. Ji, K. T. Lee and L. F. Nazar, *Nat. Mater.*, 2009, **8**, 500-506.
12 W. G. Wang, X. Wang, L. Y. Tian, Y. L. Wang and S. H. Ye, *J. Mater. Chem. A*, 2014, **2**, 4316-4323.
13 C. D. Liang, N. J. Dudney and J. Y. Howe, *Chem. Mater.*, 2009, **21**, 4724-4730.
14 G. He, X. L. Ji and L. F. Nazar, *Energy Environ. Sci.*, 2011, **4**, 2878-2883.
15 M. M. Rao, W. S. Li and E. J. Cairns, *Electrochem. Commun.*, 2012, **17**, 1-5.
16 S. Thieme, J. Brückner, I. Bauer, M. Oschatz, L. Borchardt, H. Althues and S. Kaskel, *J. Mater. Chem. A*, 2013, **1**, 9225-9234.
17 S. R. Zhao, C. M. Li, W. K. Wang, H. Zhang, M. Y. Gao, X. Xiong, A. B. Wang, K. G. Yuan,Y. Q. Huang and F.Wang, *J. Mater. Chem. A*, 2013, **1**, 3334-3339.
18 W. Ahn, K. B. Kim, K. N. Jung, K. H. Shin and C. S. Jin, *J. Power Sources*, 2012, **202**, 394-399.
19 J. Guo, Y. Xu and C. Wang, *Nano Lett.*, 2011, **11**, 4288-4294.
20 J. J. Chen, Q. Zhang, Y. N. Shi, L. L Qin, Y. Cao, M. S. Zheng and Q. F. Dong, *Phys. Chem. Chem. Phys.*, 2012, **14**, 5376-5382.
21 S. Xin, L. Gu, N. H. Zhao, Y. X. Yin, L. J. Zhou, Y. G. Guo and L. J. Wan, *J. Am. Chem. Soc.*, 2012, **134**, 18510-18513.
22 F. X. Wu, A. Magasinski and G. Yushin, *J. Mater. Chem. A*, 2014, **2**, 6064-6070.
23 J. Q. Huang, Q. Zhang, S. M. Zhang, X. F. Liu, W. C. Zhu, W. Z. Qian and F. Wei, *Carbon*, 2013, **58**, 99-106.
24 D. Wang, Y. C. Yu, W. D. Zhou, H. Chen, F. J. DiSalvo, D. A. Muller and H. D. Abruña, *Phys. Chem. Chem. Phys.*, 2013, **15**, 9051-9057.
25 C. F. Zhang, H. B. Wu, C. Z. Yuan, Z. P. Guo and X. W. Lou, *Angew. Chem. Int. Ed.,* 2012, **51**, 9730-9733.
26 Y. H. Qu, Z. A. Zhang, X. W. Wang, Y. Q. Lai, Y. X. Liu and J. Li, *J. Mater. Chem. A*, 2013, **1**, 14306-14310.
27 H. Wang, Y. Yang, Y. Liang, J. T. Robinson, Y. Li, A. Jackson, Y. Cui and H. Dai, *Nano Lett.*, 2011, **11**, 2644-2647.
28 H. Xu, Y. F. Deng, Z. C. Shi, Y. X. Qian, Y. Z. Meng and G. H. Chen, *J. Mater. Chem. A*, 2013**, 1**, 15142-15149.
29 L. Ji, M. Rao, H. Zheng, L. Zhang, Y. Li, W. Duan, J. Guo, E. J. Cairns and Y. Zhang, *J. Am. Chem. Soc.*, 2011, **133**, 18522-18525.
30 N. W. Li, M. B. Zheng, H. L. Lu, Z. B. Hu, C. F. Shen, X. F. Chang, G. B. Ji, J. M. Cao and Y. Shi, *Chem. Commun.*, 2012, **48**, 4106-4108.
31 M. S. Park, J. S. Yu, K. J. Kim, G. Jeong, J. H. Kim, Y. N. Jo, U. Hwang, S. Kang, T. Woo and Y. J. Kim, *Phys. Chem. Chem. Phys.*, 2012, **14**, 6796-6804.
32 C. Wang, K. Su, W. Wan, H. Guo, H. H. Zhou, J. T. Chen, X. X. Zhang and Y. H. Huang, *J. Mater. Chem. A*, 2014, **2**, 5018-5023.
33 L. Q. Lu, L. J. Lu and Y. Wang, *J. Mater. Chem. A*, 2013, **1**, 9173-9181.
34 B. Ding, C. Z. Yuan, L. F. Shen, G. Y. Xu, P. Nie, Q. X. Lai and X. G. Zhang, *J. Mater. Chem. A*, 2013, **1**, 1096-1101.
35 H. B. Zhao, Z. H. Peng, W. J. Wang, X. K. Chen, J. H. Fang and J. Q. Xu, *J. Power Sources,* 2014, **245**, 529-536.
36 M. K. Song, Y. G. Zhang and E. J. Cairns, *Nano Lett.*, 2013, **13**, 5891-5899.
37 L. Zhou, X. J. Lin, T. Huang and A. S. Yu, *J. Mater. Chem. A*, 2014, **2**, 5117-5123.
38 X. D. Huang, B. Sun, K. F. Li, S. Q. Chen and G. X. Wang, *J. Mater. Chem. A*, 2013, **1**, 13484-13489.
39 M. Xiao, M. Huang, S. S. Zeng, D. M. Han, S. J. Wang, L. Y. Sun and Y. Z. Meng, *RSC Adv.*, 2013, **3**, 4914-4916.
40 T. Q. Lin, Y. F. Tang, Y. M. Wang, H. Bi, Z. Q. Liu, F. Q. Huang, X. M. Xie and M. H. Jiang, *Energy Environ. Sci.*, 2013, **6**, 1283-1290.
41 G. M. Zhou, L. C. Yin, D. W. Wang, L. Li, S. F. Pei, I. R. Gentle, F. Li and H. M. Cheng, *ACS Nano*, 2013, **7**, 5367-5375.
42 H. Bai, C. Li and G. Shi, *Adv. Mater.*, 2011, **23**, 1089-1115.
43 Z. S. Wu, G. M. Zhou, L. C. Yin, W. Ren, F. Li and H. M. Cheng, *Nano Energy*, 2012, **1**, 107-131.
44 C. H. Xu, B. H. Xu, Y. Gu, Z. G. Xiong, J. Sun and X. S. Zhao, *Energy Environ. Sci.*, 2013, **6**, 1388-1414.
45 S. Evers and L. F. Nazar, *Acc. Chem. Res.*, 2013, **46**, 1135-1143.
46 L. Zhang, L. Ji, P. A. Glans, Y. Zhang, J. Zhu and J. Guo, *Phys. Chem. Chem. Phys.*, 2012, **14**, 13670-13675.
47 S. E. Cheon, K. S. Ko, J. H. Cho, S. W. Kim, E. Y. Chin and H. T. Kim, *J. Electrochem. Soc.*, 2003, **150**, A796-A799.
48 S. S. Zhang, *J. Power Sources*, 2013, **231**, 153-162.
49 Y. L. Cao, X. L. Li, I. A. Aksay, J. Lemmon, Z. M. Nie, Z. G. Yang and J. Liu, *Phys. Chem. Chem. Phys.*, 2011, **13**, 7660-7665.
50 G. Q. Ma, Z. Y. Wen, J. Jin, Y. Lu, K. Rui, X. W. Wu, M. F. Wu and J. C. Zhang, *J. Power Sources*, 2014, **254**, 353-359.
51 F. Wu, J. Chen, R. Chen, S. Wu, L. Li, S. Chen and T. Zhao, *J. Phys. Chem. C*, 2011, **115**, 6057-6063.
52 Y. Yang, G. Yu, J. J. Cha, H. Wu, M. Vosgueritchian, Y. Yao, Z. Bao and Y. Cui, *ACS Nano*, 2011, **5**, 9187-9193.
53 F. Wu, J. Chen, L. Li, T. Zhao and R. Chen, *J. Phys. Chem. C*, 2011, **115**, 24411-24417.
54 G. C. Li, G. R. Li, S. H. Ye and X. P. Gao, *Adv. Energy Mater.*, 2012, **2**, 1238-1245.
55 W. D. Zhou, Y. C. Yu, H. Chen, F. J. DiSalvo and H. D. Abruña, *J. Am. Chem. Soc.*, 2013, **135**, 16736-16743.
56 M. J. Wang, W. K. Wang, A. B. Wang, K. G. Yuan, L. X. Miao, X. L. Zhang, Y. Q. Huang, Z. B. Yu and J. Y. Qiu, *Chem. Commun.*, 2013, **49**, 10263-10265.
57 Y. Z. Fu and A. Manthiram, *Chem. Mater.*, 2012, **24**, 3081-3087.
58 Y. Z. Fu and A. Manthiram, *J. Phys. Chem. C*, 2012, **116**, 8910-8915.

Journal of Materials Chemistry A Accepted Manuscript

59 Y. W. Zhu, S. Murali, M. D. Stoller, K. J. Ganesh, W. W. Cai, P. J. Ferreira, A. Pirkle, R. M. Wallace, K. A. Cychosz, M. Thommes, D. Su, E. A. Stach and R. S. Ruoff, *Science*, 2011, **332**, 1537-1541.

60 L. L. Zhang, X. Zhao, M. D. Stoller, Y. W. Zhu, H. X. Ji, S. Murali, Y. P. Wu, S. Perales, B. Clevenger and R. S. Ruoff, *Nano Lett.*, 2012, **12**, 1806-1812.

61 J. L. Shen, C. Y. Yang, X. W. Li and G. C. Wang, *ACS Appl. Mater. Interfaces*, 2013, **5**, 8467-8476.

62 W. S. Hummers and R. E. Offeman, *J. Am. Chem. Soc.*, 1958, **80**, 1339-1341.

63 Y. Q. Han, Y. Lu, *Synth. Met.*, 2008, **158**, 744-748.

64 W. Y. Li, G. Y. Zheng, Y. Yang, Z. W. Seh, N. Liu and Y. Cui, *Proc. Natl. Acad. Sci.*, 2013, **110**, 7148-7153.

65 W. Y. Li, Q. F. Zhang, G. Y. Zheng, Z. W. Seh, H. B. Yao and Y. Cui, *Nano Lett.*, 2013, **13**, 5534-5540.

66 A. T. Ward, *J. Phys. Chem.*, 1968, **72**, 4133-4139.

67 X. G. Yu, J. Y. Xie, J. Yang, H. J. Huang, K. Wang and Z. S. Wen, *J. Electroanal. Chem.*, 2004, **573**, 121-128.

68 J. Fanous, M. Wegner, J. Grimminger, M. Rolff, M. B. M. Spera, M. Tenzer and M. R. Buchmeiser, *J. Mater. Chem.*, 2012, **22**, 23240-23245.

69 J. J. Xu, K. Wang, S. Z. Zu, B. H. Han and Z. X. Wei, *ACS Nano*, 2010, **4**, 5019-5026.

70 X. Y. Tao, J. T. Zhang, Y. Xia, H. Huang, J. Du, H. Xiao, W. K. Zhang and Y. P. Gan, *J. Mater. Chem. A*, 2014, **2**, 2290-2296.

71 B. Jin, J. U. Kim and H. B. Gu, *J Power Sources*, 2003, **117**, 148-152.

72 H. Sun, G. L. Xu, Y. F. Xu, S. G. Sun, X. F. Zhang, Y. C. Qiu and S. H. Yang, *Nano Res.*, 2012, **5**, 726-738.

73 S. S. Zhang, *Electrochim. Acta*, 2012, **70**, 344-348.

74 S. S. Zhang, *J. Electrochem. Soc.*, 2012, **159**, A920-A923.

Journal of Materials Chemistry A Accepted Manuscript

This journal is © The Royal Society of Chemistry [year]